Chapter 5
3D Printing Approaches for Reproducible Measurement of Vibroacoustically Excited Triboelectric Nanogenerators

Nakul S. Deshpande*, Eric C. Bryant*, Thomas Z. Box, Thomas S. Cox, Audrey L. Evans, Natalie White, Kent X. Eng, Stephen J. Kao, Darrel T. Beckman, Christopher A. Mizzi, Luke B. Beardslee, and Amanda E. King

Abstract Triboelectric nanogenerators (TENGs) are a rapidly growing technology with applications ranging from energy harvesting to vibrational sensing. In this work, we present a method to quantify the voltage output of TENGs upon vibroacoustic excitation via the use of rigid, 3D-printed fixtures. Our goal in utilizing such fixtures was to mitigate or eliminate the deleterious effect of buckling deformations on the performance of our TENGs. The developed fixture features a beveled ring that presses into the clamped membrane and allows us to qualitatively tension the films. Vibrational modes from films in this fixture become highly reproducible. We complement our experiments with a continuum formulation to quantify the influence of the printed fixtures on the membrane tension within the TENG. Tensioning thin films to modify voltage generation within frequency ranges opens future possibilities for tuning TENG performance via device design.

Introduction

Triboelectric nanogenerators are an emerging vibrational energy harvesting technology. At their most basic level, TENGs are easily constructed by affixing two dielectric films that have been coated on one side with an electrode material (Fig. 1). Any motion that causes friction within the interstitial space creates a tribo-generated charge that can subsequently be used in either energy harvesting or vibrational sensing techniques. Numerous research groups have collectively demonstrated that TENGs can be made from a wide variety of dielectric materials. Since their initial disclosure, TENGs have found a wide suite of applications [1] ranging from devices used to measure humidity and airflow [2] and to harvest energy from the environment (in the form of waves and wind) [3], in wearable and soft robotics [4], and in mobile electronics and biomechanical applications [5]. This wide plethora of applications rely on mechanical inputs to the TENG that result in one of two modes of activation: clapping (i.e., separation-contact) and lateral sliding.

Nakul S. Deshpande · Eric C. Bryant · Thomas Z. Box · Thomas S. Cox · Audrey L. Evans · Darrel T. Beckman · Christopher A. Mizzi · Amanda E. King(✉)
Los Alamos National Laboratory
e-mail: ndeshpande@lanl.gov; ecbryant@lanl.gov; tbox@lanl.gov; tscox@lanl.gov; audreyevans@lanl.gov; dbeckman@lanl.gov; mizzi@lanl.gov; aeking@lanl.gov

Natalie White
Brigham Young University
e-mail: njwhite219@gmail.com

Kent X. Eng
Princeton University
e-mail: ke9722@princeton.edu

Stephen J. Kao
University of New Mexico
e-mail: tundra@unm.edu

Luke B. Beardslee
Silixa LLC
e-mail: luke.b.beardslee@gmail.com

Kristin B. Zimmerman, PhD (eds.), *Topics in Modal Analysis & Parameter Identification in Structural Dynamics, 2026, Vol. 8*, Conference Proceedings of the Society for Experimental Mechanics Series, https://doi.org/10.1007/978-8-743-81447-4_5

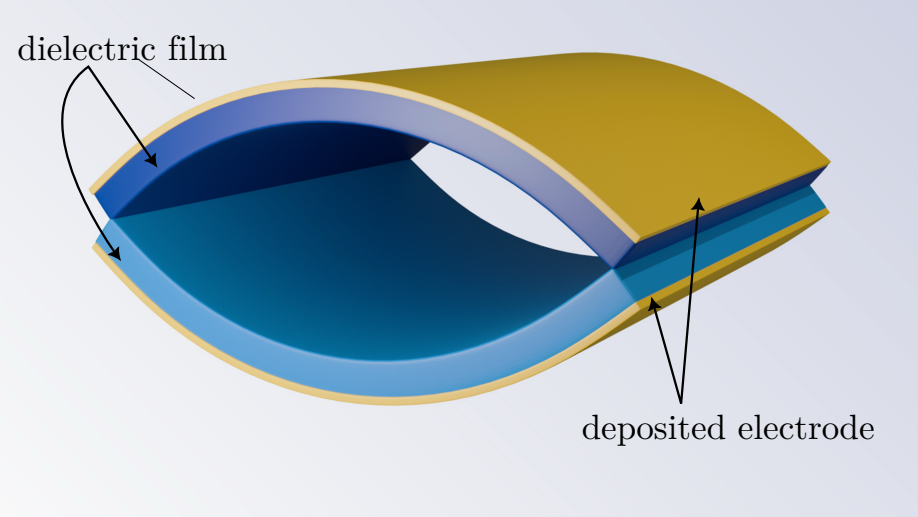

Fig. 1 TENG schematic. TENGs consist of two dielectric films, coated with an electrode, and brought into frictional contact

While TENGs have been extensively researched and new form factors are disclosed regularly, the TENG community has not, to date, established standardized testing metrics and figures of merit (FOM) that allow quantitative comparisons across the wide catalog of current and future TENG packages [6]. Assessing TENG performance has generally relied on measurements of the output voltage alone [7] without considering neither the effect of the type and strength of the mechanical energy input [8] nor how the TENG was affixed to a test surface. In this study, we develop and test 3D-printed testing fixtures that enable the reproducible testing of TENGs and propose coherence analysis as an approach to ultimately permit the quantitative comparison of TENGs of differing form factors.

Methods

Experimental Methods

3D-printing of fixtures. Fixtures were designed in SolidWorks, and printed using a Formlabs Fuse 1+ 3D printer, using Nylon 12.

Construction of TENGs. TENGs were constructed by placing electrode-coated films in the 3D-printed fixtures such that the uncoated sides were in contact. Selected dielectric films are shown in Table 1, and were purchased from McMaster Carr. The films were cut into predetermined shapes using a Cricut Maker 3 prior to being coated with ∼70 nm of gold via physical vapor deposition techniques.

Testing. All testing efforts, regardless of films tested, involved vibroacoustic excitation using a linear acoustic chirp (0.001 Hz to 4000 Hz in 0.2 s) provided by a speaker. The deformation resulting from vibroacoustic excitation was measured with a PolytecTM laser Doppler vibrometer (LDV) to quantify the magnitude and phase of the velocity at the surface of the tested films at discrete points (N ∼ 800). Velocity is measured in the frequency domain within a span of 0.001 Hz to 4000 Hz, with a Fast Fourier Transform (FFT) bin resolution of 5 Hz. Single films, as well as double film combinations (i.e., two films that were lacking a gold electrode), were measured in this manner after emplacing them in a fixture. In addition to being interrogated by LDV measurements, TENGs were subjected to voltage measurements upon vibroacoustic excitation. Leads were connected to a NI DAQ Sound and Vibration Device, NI USB-4432). A calibrated microphone placed approximately 10 cm away from the face of the TENG provided a means of calculating the vibroacoustic coherence of the TENGs according to the following equations:

$$C_{xy} = \frac{P_{xy}^2}{P_{xx} * P_{yy}}, \quad P(\nu) = \frac{1}{K}\sum_{k=1}^{K} P_k(\nu) \tag{1}$$

where P_{xx} and P_{yy} are power spectral density estimates of time-series data x and y, and P_{xy} is the cross spectral density estimate of inputs x and y [9]. Note that the power-spectral-density operator, $P(\nu)$, maps $\nu = \frac{i}{M}$ for $-(\frac{M}{2} - 1) \leq i \leq \frac{M}{2}$,

where the windowing parameter M is the number of data points in each segment of the power spectral density estimate. Microphone and TENG output voltage data were collected for 10 s, resulting in the collection of data from 50 chirps.

Table 1 Tested polymer films. All films are sourced from McMaster-Carr, and are cut to the dimensions of the fixtures

Polymer	**Thickness** (μm)
Kapton	25, 76
Polyethylene (PE)	101, 254
Polyethylene terephthalate (PET)	76
Polytetrafluoroethylene (PTFE)	76
Polyvinyl chloride (PVC) : Unplasticized	127
Polyvinyl chloride (PVC) : Plasticized	406
Polyvinylidene fluoride (PVDF)	76, 254

Numerical Methods

We performed frequency domain structural dynamics simulations in COMSOL [10], generally following canonical formulations [11]. To model the response and behavior of single films, double film combinations, and TENGs, these simulations require (1) the elastic material properties and (2) the initial state. Material properties are selected from those reported by McMaster-Carr of the polymer films, while the initial strain field is first applied, then adjusted such that that simulation solution matches the experimentally measured peaks of the FFT.

Results and Discussion

Our work was motivated by the current lack of both standardized testing methods and FOM approaches in the TENG literature. The postulation that enclosing the TENG would lead to reproducible measurements was tested by encasing the TENG within a rigid 3D-printed fixture and subsequently exciting the TENG with a vibroacoustic chirp. Vibroacoustic measurements present several advantages: they are nondestructive, easily reproducible, and can be quickly executed. To disentangle the contributions due to potential interactions between the two films of our TENGs, we measured the vibroacoustic response of single films and verified our experimental results using a numerical model. In total, we measured the vibroacoustic response of ten polymer thin films (Table 1) and the voltage response of fourteen thin film combinations. Multiplicative combinations of thin films restrict the volume of data we can show, and thus we focus below on salient results to avoid redundancy.

Vibroacousitcs of single films in square and circular fixtures

Our initial efforts focused on employing square fixtures. A representative vibroacoustic response of a square film (127 μm thick PVC) is shown in (Fig. 2). Numerous sharp peaks are evident between 0 and 50 Hz; due to their lower spectral power, these peaks are interpreted as noise. We observe similar peaks in the same frequency range for all tested films when employing the square fixtures. In PVC, the first vibrational mode appears as a single prominent peak at 670 Hz. The spatial map of the first vibrational mode reveals a single amplitude peak located within the center of the film. The second and third vibrational modes appear at 1560 Hz and 1620 Hz, respectively; the spatial map reveals three amplitude peaks in both the second and third vibrational modes, with the features rotated 90 degrees from each other. The fourth mode occurs at 1915 Hz and visually has four amplitude peaks placed in a square formation around a central feature. The fifth mode occurs at 2440 Hz, and the spatial map reveals five amplitude peaks arranged along the diagonal of the square (Fig. 2).

Thin films enclosed in circular fixtures exhibit the first five vibrational modes at frequencies less than 500 Hz. Peaks of these modes are sharp and closely spaced. A representative vibroacoustic response of a circular film (254 μm thick PE) is shown in (Fig. 2). The first vibrational mode occurs at 140 Hz and has as an off-center amplitude peak. The second and third vibrational modes occur at 205 and 250 Hz, respectively, and have two amplitude peaks rotated 90 degrees from each other. The fourth vibrational mode occurs at 325 Hz and exhibits a quadrupolar symmetry. The fifth vibrational mode occurs at 465 Hz and appears to have six amplitude peaks surrounding a seventh peak.

Classical structural dynamics relationships [11] reproduce the experimental phenomenology observed above, albeit with important differences between the square and circular fixtures. Simulations conducted in the square geometry reproduce the

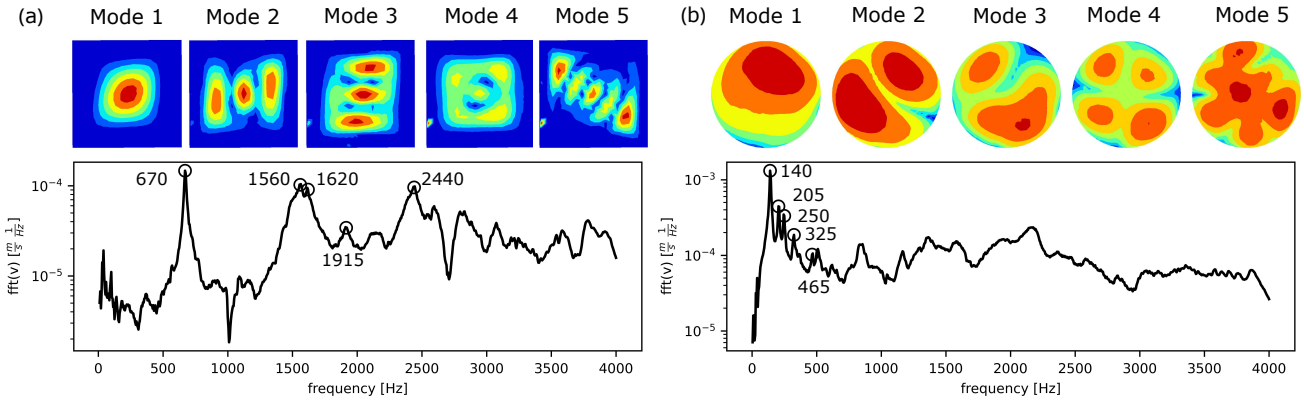

Fig. 2 Experimental vibroacoustic phenomenology: Spatial maps of the first five vibrational modes (top row), identified from peaks in the FFT (bottom row), for (a) PVC 127μm in a square fixture and (b) PE 254 μm in a circular fixture. Open circles in the FFT indicate peaks. Both experimental results come from measurements on clamped, un-tensioned single films

observed modal shapes: a single amplitude peak in the first vibrational mode, two amplitude peaks rotated from each other in the second and third vibrational modes, and four-fold symmetric distribution of amplitude peaks in the fourth vibrational mode. The calculated frequencies at which the modes occur do not match the experimentally measured values. We attribute this mismatch to both the inherent anisotropy of the material and the potential inconsistencies when initially tensioning the film. However, we could more accurately predict the frequency of the vibrational modes when the peaks were fitted independently of each other.

The inability to accurately predict the vibrational frequencies of the observed modal shapes of films in square fixtures prompted us to move towards circular test fixtures, which could be more accurately predicted (Fig. 3, Table 2). These efforts demonstrate that the initial choice of a coordinate system, dictated by the initial selection of fixture design, prescribes the ability to match experiment with modeling. Other key parameters that influence modeling efforts include material properties, initial strain within the fixture, and boundary tension. Because material properties do not significantly change during loading

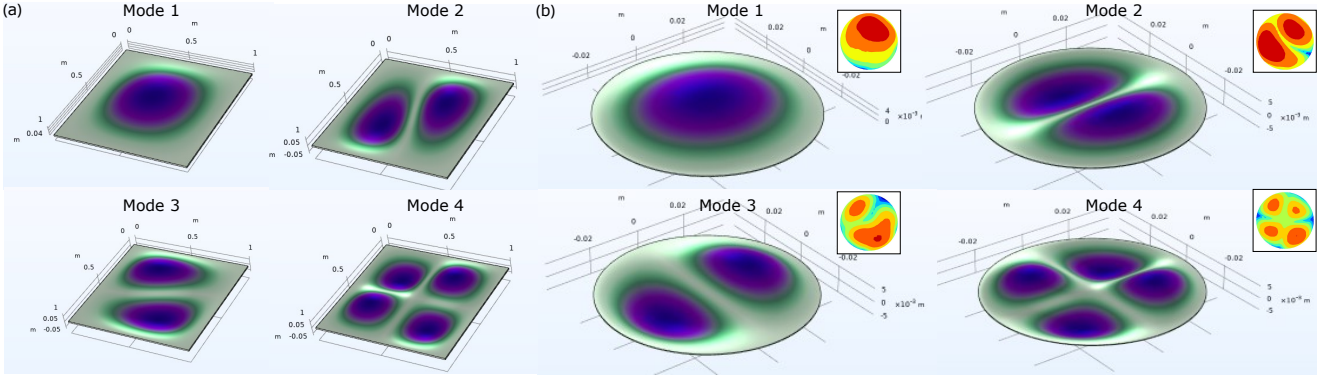

Fig. 3 Simulated vibroacoustic responses. Experimental vs. simulated vibrational modes for (a) PVC 406 μm in a square fixture and (b) PVDF 254 μm in a circular fixture. Insets of simulation results indicate experimental results at the same modes

Table 2 Experimental vs. simulated modal frequencies for PVC 406 μm in a square fixture and PVDF 254 μm in a circular fixture

	Square				**Circle**			
Mode	1	2	3	4	1	2	3	4
Vibrometer frequency (Hz)	518	787	853	1096	229	297	353	459
FEA frequency (Hz)	503	793	835	1051	206	307	377	445

within the fixture or during vibroacoustic testing, the discrepancies between experiment and simulation likely originate in stresses imposed by emplacing the film within the fixture. Rectifying these discrepancies will rely on accurate measurement of the initial film strain within the fixture and proper treatment of the boundary conditions. To ultimately apply these insights to TENGs, we envision extending our employed simulation methods [11] to multi-film systems. Such approaches could include numerical methods for Lagrangian overlap coupling [12], as such overlap coupling is currently unavailable in commercial finite element analysis packages such as COMSOL. We are currently developing such capabilities in our laboratories.

Vibroacoustics of dual film systems in circular fixtures

After establishing the general behavior of vibrating single films and calibrating a corresponding numerical model, we moved to dual film assemblies. The experimental study of dual film assemblies presents a key question: do both films, when in contact with each other, exhibit comparable vibroacoustic responses with respect to mode shapes and resonant frequencies? If comparable vibroacoustic responses are observed, the implication is that an interaction between both films is occurring and thus needs to be incorporated into any numerical modeling approach. The experimental challenge became the design of a fixture that could independently clamp, tension, and connect the films (Fig. 4).

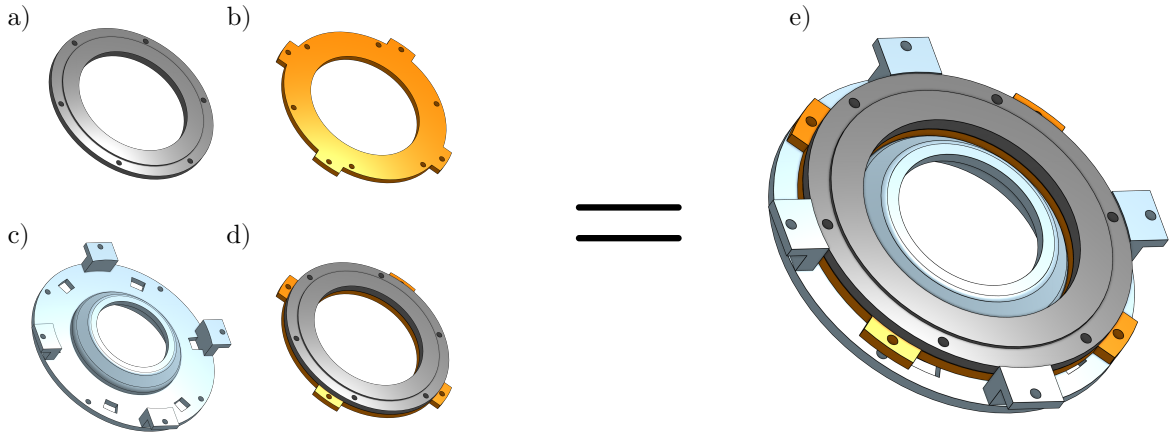

Fig. 4 3D printed fixture components. (a) Base plate. (b) Top ring. (c) Base for tension (d) Clamped configuration. (e) Clamped and tensioned configuration. Tension is administered to the film by the indentation of component c) which presses the film

When clamped, untensioned films are brought into contact, their vibroacoustic responses have some weak overlap at low frequencies and little similarity at high frequencies (Fig. 5). However, when tension is applied by pressing component c) into the film (Fig. 4), the vibroacoustic response of both films are brought into agreement, with a high degree of overlap across the entire frequency range (Fig. 5).

Quantifying the response of TENGs using coherence as a FOM

There currently exists a lack of standardized metrics and FOMs for characterizing the performance of TENGs. In a vast majority of literature reports on these devices, TENGs are not measured relative to standard instruments such as accelerometers or microphones; this knowledge gap has arguably prevented TENGs from being more widely adopted in vibrational energy harvesting and vibrational sensing applications. In this initial effort, we focused on characterizing the voltage response of TENGs as a function of frequency and evaluating our results against a calibrated microphone. Such efforts could have implications in designing TENGs well-matched to vibrational energy harvesting from systems that exhibit persistent, characteristic vibrational frequencies (e.g., the swaying motion of a bridge or energy harvesting systems in hybrid vehicles).

Use of a calibrated microphone allowed us to utilize coherence to quantitatively compare TENGs emplaced in circular fixtures (Fig. 6). Coherence is a statistical measurement that quantifies the linear correlation between two signals in the frequency domain; a value of 1 indicates perfect linear correlation, while a value of 0 indicates no correlation at all at a specific frequency. For most of our tested TENG combinations, coherence increases as the input vibrational frequency increases. Coherence is highly sensitive to the choice of parameter M (the length of the time-series segment over which the

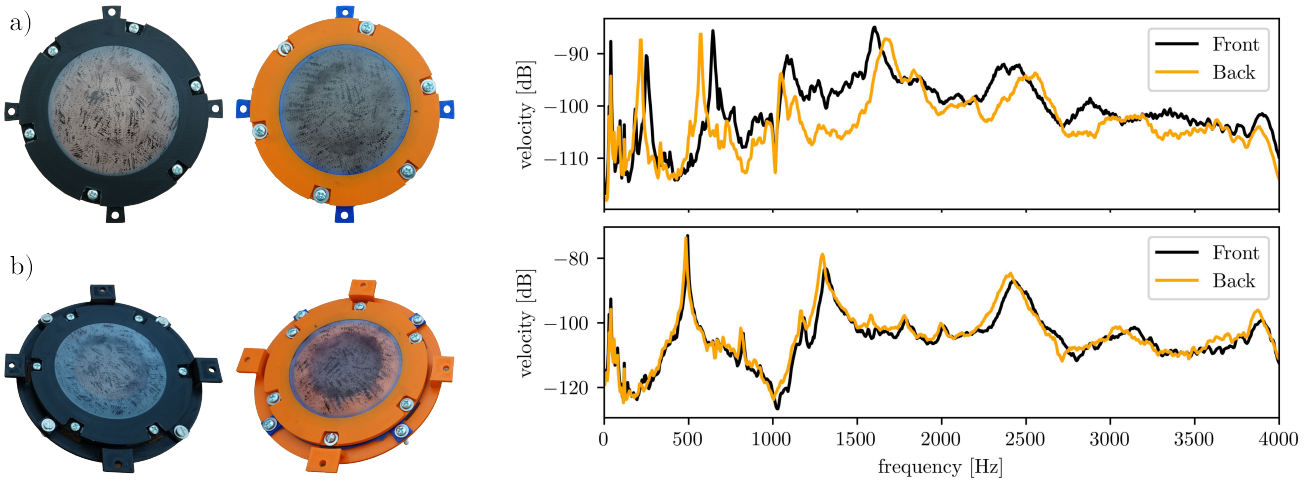

Fig. 5 Behavior of clamped and tensioned films. (a) Top row indicates clamped configuration and vibroacoustic response (b) Bottom row indicates clamped and tensioned configuration. Note that tensioned samples show consistent, repeatable FFT responses both in double-flim geometries and across experimental realizations

power spectral density is computed). We observe an increase in coherence as the parameter M (the length of the time-series segment over which the power spectral density is computed) is increased. Averaging the coherence values across the input frequency range yields the data shown in Fig. 7. This plot suggests that the pairings of Kapton and PE in a TENG is the most promising TENG for applications involving vibrational frequencies between 0 and 4000 Hz, while pairings of 254 μm thick PVDF with Kapton would be poor harvesters and sensors in similar applications.

Our work indicates that vibroacoustic coherence is a potential FOM to systematically characterize and benchmark the performance of TENG devices. This method can be used to identify optimal TENG design parameters and aid in identifying those parameters that dictate the mechanisms governing TENG performance. The latter is crucial because TENG applica-

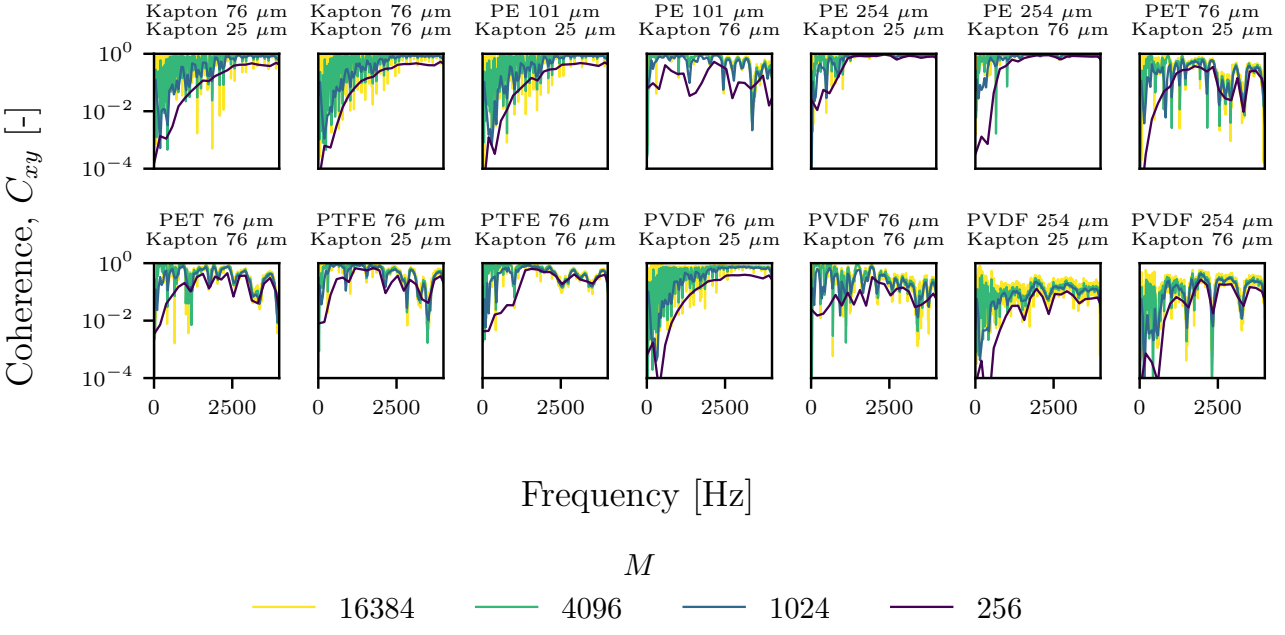

Fig. 6 Summary TENG coherence. Each panel indicates a unique TENG configuration and the corresponding coherence measure. Coherence is computed between a microphone recording of the chirp signal and the voltage output of the indicated TENG combination. Colors indicate varying values of the parameter M

tions continue to grow, but the mechanisms underpinning their operation remain elusive [13]. For example, the triboelectric effect — the phenomenon by which rubbing two materials together causes charge to transfer between them [14] — is central to TENGs, but is still not fully understood despite having been known for at least 2500 years [15]. In part, this is because triboelectricity is a complex process [16] likely involving multiple charged species [17] whose transfer is driven by some combination of electromechanical [18] and/or thermal [19] factors. We anticipate that vibroacoustic coherence characterization of TENGs, paired with more local measurements, can be applied to gain insights into these basic research questions.

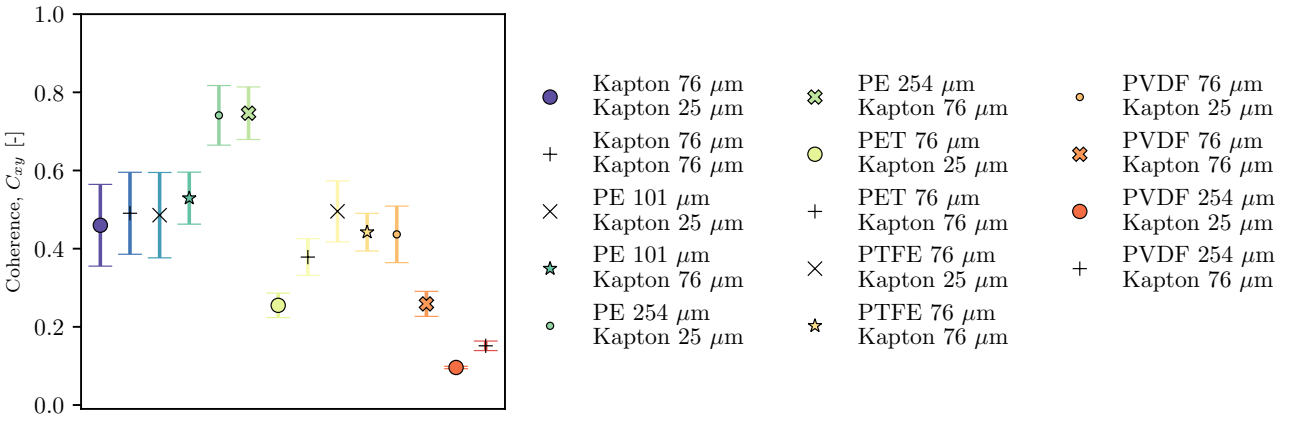

Fig. 7 Frequency averaged vibroacoustic coherence of tested TENG devices. Mean and variance of coherence for all tested films. Each marker indicates a unique TENG combination, errorbars indicate the variance of C_{xy} computed across the frequency domain of 0-4000 Hz

Conclusions

Our goals in this work were to demonstrate a robust experimental workflow in fabricating TENG devices, to demonstrate the basic validity of linearized elastic structural dynamics, and to propose vibroacoustic coherence as a FOM to quantify the output performance of TENG devices. We found that combinations of Kapton and PE provide the highest degree of coherence, and that the choice of experimental geometries strongly influences the details of the numerical simulations. Simply moving from a square to a circular geometry allowed for the prediction and match of the peak resonant frequencies as well as the spatial maps of the vibrational modes. Finally, we found that the benefit of vibroacoustic coherence is its simplicity. It is experimentally tractable, via an accessible acoustics-based workflow. With the plethora of driving mechanisms that exist in TENG response, a single metric agnostic to the nature of the excitation source that can relate input to output is extremely useful in comparing TENGs across many applications.

Previous research has called into question the ability of TENGs to behave reproducibly both as a function of time and between TENGs made of identical materials. Explanations for observed deviations in performance include temperature and humidity. During execution of our work, we have found that controlling tension within the fixtures leads to more consistent experimental results, and we postulate that this parameter has been a neglected consideration in the evaluation of TENG performance in previously published studies. Additionally, there are several caveats to TENG performance indicated in the comparison in (Fig. 7). For instance, the manufacturing process of thin polymeric materials likely alters their linearized electro-elastodynamic parameters. While the material parameters reported by manufacturers are accurate to a degree, the variability resulting from differences in manufacturing processes is significant enough to be considered in how the simulations match the experiments. In future work, stronger control over the fabrication of the polymers themselves would be beneficial and could provide independent measurements of the materials.

In future simulations, our reformulation is now amenable to additional energetic contributions that enforce damped cross-domain interactions for multi-film and film-fixture contact – as characterized either by a displacement jump or an overlap coupling method [20, 12]. An FEA-prescribed initial stress-based initialization [21] has been preliminary vetted (as, thus far, intrinsically necessary for thin-film calibration): initial stress may perform differently than in prior COMSOL modeling. Stepping towards fully-resolved multiphysics numerical simulations relies upon a robust experimental workflow and numerical simulations that are physically justified. However, we note that charge generation and transport is not a

phenomenon unique to TENGs. Each mode of deformation has been linked or inferred to activate a different physical source of voltage generation [22]. This knowledge should be coupled with growing recognition of and capabilities for simulating the electrodynamics [23] for a complete picture of TENG deformation and charge generation.

References

1. Prabhakar Yadav et al. “Applications of Multifunctional Triboelectric Nanogenerator (TENG) Devices: Materials and Prospects”. Sustainable Energy & Fuels 7.16 (2023), pp. 3796–3831. DOI: 10.1039/D3SE00714F.
2. Vu Nguyen and Rusen Yang. “Effect of Humidity and Pressure on the Triboelectric Nanogenerator”. Nano Energy 2.5 (Sept. 2013), pp. 604–608. DOI: 10.1016/j.nanoen.2013.07.012.
3. Xiaonan Wen et al. “Harvesting Broadband Kinetic Impact Energy from Mechanical Triggering/Vibration and Water Waves”. ACS Nano 8.7 (July 2014), pp. 7405–7412. DOI: 10.1021/nn502618f.
4. Min Pan et al. “Triboelectric and Piezoelectric Nanogenerators for Future Soft Robots and Machines”. iScience 23.11 (Nov. 2020), p. 101682. DOI: 10.1016/j.isci.2020.101682.
5. Xiaole Cao et al. “Multidiscipline Applications of Triboelectric Nanogenerators for the Intelligent Era of Internet of Things”. Nano-Micro Letters 15.1 (Dec. 2022), p. 14. DOI: 10.1007/s40820-022-00981-8.
6. Daniel M. Mulvihill et al. “How to Test Triboelectric Nanogenerators: Key Factors for Standardized Performance Evaluation”. Advanced Energy Materials (Aug. 2025), e02920. DOI: 10.1002/aenm.202502920.
7. Sihong Wang, Long Lin, and Zhong Lin Wang. “Nanoscale Triboelectric-Effect-Enabled Energy Conversion for Sustainably Powering Portable Electronics”. Nano Letters 12.12 (Dec. 2012), pp. 6339–6346. DOI: 10.1021/nl303573d.
8. Simiao Niu et al. “Theoretical Investigation and Structural Optimization of Single-Electrode Triboelectric Nanogenerators”. Advanced Functional Materials 24.22 (June 2014), pp. 3332–3340. DOI: 10.1002/adfm.201303799.
9. P. Welch. “The Use of Fast Fourier Transform for the Estimation of Power Spectra: A Method Based on Time Averaging over Short, Modified Periodograms”. IEEE Transactions on Audio and Electroacoustics 15.2 (June 1967), pp. 70–73. DOI: 10.1109/TAU.1967.1161901.
10. COMSOL Multiphysics®. COMSOL AB, Stockholm, Sweden.
11. Subrata Mukherjee. “Variational Principles in Dynamic Thermoviscoelasticity”. International Journal of Solids and Structures 9.10 (Oct. 1973), pp. 1301–1316. DOI: 10.1016/0020-7683(73)90116-9.
12. S. P. Xiao and T. Belytschko. “A Bridging Domain Method for Coupling Continua with Molecular Dynamics”. Computer Methods in Applied Mechanics and Engineering 193.17 (May 2004), pp. 1645–1669. DOI: 10.1016/j.cma.2003.12.053.
13. Zhong Lin Wang. “From Contact Electrification to Triboelectric Nanogenerators”. Reports on Progress in Physics 84.9 (Sept. 2021), p. 096502. DOI: 10.1088/1361-6633/ac0a50.
14. Daniel J. Lacks and R. Mohan Sankaran. “Contact Electrification of Insulating Materials”. Journal of Physics D: Applied Physics 44.45 (Oct. 2011), p. 453001. DOI: 10.1088/0022-3727/44/45/453001.
15. Paul Iversen and Daniel J. Lacks. “A Life of Its Own: The Tenuous Connection between Thales of Miletus and the Study of Electrostatic Charging”. Journal of Electrostatics 70.3 (June 2012), pp. 309–311. DOI: 10.1016/j.elstat.2012.03.002.
16. L. D. Marks and K. P. Olson. “Flexoelectricity, Triboelectricity, and Free Interfacial Charges”. Small, p. 2310546. DOI: 10.1002/smll.202310546.
17. Giulio Fatti et al. “Uncertainty and Irreproducibility of Triboelectricity Based on Interface Mechanochemistry”. Physical Review Letters 131.16 (Oct. 2023), p. 166201. DOI: 10.1103/PhysRevLett.131.166201.
18. C. A. Mizzi, A. Y. W. Lin, and L. D. Marks. “Does Flexoelectricity Drive Triboelectricity?” Physical Review Letters 123.11 (Sept. 2019), p. 116103. DOI: 10.1103/PhysRevLett.123.116103.
19. Eui-Cheol Shin et al. “Derivation of a Governing Rule in Triboelectric Charging and Series from Thermoelectricity”. Physical Review Research 4.2 (May 2022), p. 023131. DOI: 10.1103/PhysRevResearch.4.023131.
20. Alexander Lindsay et al. “Automatic Differentiation in MetaPhysicL and Its Applications in MOOSE”. Nuclear Technology 207.7 (July 2021), pp. 905–922. DOI: 10.1080/00295450.2020.1838877.
21. Guancong Ma et al. “Acoustic Metasurface with Hybrid Resonances”. Nature Materials 13.9 (Sept. 2014), pp. 873–878. DOI: 10.1038/nmat3994.
22. Daniel Moreno-Garcia, Kaitlin M Howell, and Luis Guillermo Villanueva. “Flexoelectricity in Amorphous Hafnium Oxide (HfO2)”.
23. Shengquan Li et al. “Numerical Simulations of Piezoelectricity and Triboelectricity: From Materials, Structures to Devices”. Applied Materials Today 37 (Apr. 2024), p. 102092. DOI: 10.1016/j.apmt.2024.102092.